Korean J. Chem. Eng., 39(8), 2055-2068 (2022)
DOI: 10.1007/s11814-022-1121-4

pISSN: 0256-1115
eISSN: 1975-7220

The effects of under-ribs convection on enhanced drainage parallel flow field for proton exchange membrane fuel cell

Sida Wu*, Weimin Yang*,,***,†, Jin Zhan*,†, Hua Yan*, Xianghao Kong*, and Xiahua Zuo***

*College of Mechanical and Electronic Engineering, Beijing University of Chemical Technology, Beijing 100029, China
**State Key Laboratory of Organic-Inorganic Composities, College of Material Science and Engineering, Beijing University of Chemical Technology, Beijing 100029, China
***Beijing Adavanced Innovation Center for Soft Matter Science and Engineering, Beijing University of Chemical Technology, Beijing 100029, China
(*Received 8 November 2021 • Revised 17 February 2022 • Accepted 20 March 2022*)

Abstract−A new enhanced drainage parallel (EDP) flow field was designed that not only enhances under-rib convection but also enables a more uniform distribution of hydrogen and oxygen. Through the optimization of the model, we established the influence of the flow field size, relative humidity, and stoichiometric ratio on cell performance. When the rib width is reduced, the maximum power density is improved. Compared with the parallel flow field and serpentine flow field, the maximum power density of the EDP flow field was increased by 69.4% and 7.9%, respectively. Under optimal conditions, the net power of the EDP flow field can reach 0.56 W/cm^2. In the single-cell test, the maximum power density of the EDP flow field can reach 1.19 W/cm^2. This implies that the EDP flow field has potential application of proton exchange membrane fuel cells.

Keywords: Proton Exchange Membrane Fuel Cell, Flow Field, Water Management, Fuel Cell, Water Transport

INTRODUCTION

In recent years, there has been an increasing interest in proton exchange membrane fuel cells (PEMFCs). During the operation of PEMFC, the only by-product is water. At the same time, it also has many advantages, such as quick start-up, high energy utilization, and lower operating temperature [1-3]. These potentials make it a favorable competitor for traditional fossil energy. PEMFC is a clean energy device that converts the chemical energy stored in the reaction gas into electrical energy by redox reactions [4,5]. Single-cell is mainly composed of bipolar plate (BPP), gas diffusion layer (GDL), catalyst layer (CL), and proton exchange membrane.

As a key component of the fuel cells, the bipolar plate is responsible for separating the anode and cathode, equally dividing the reaction gas, discharging the by-product water, conducting electrons, and providing mechanical support for the cells. In addition, BPP occupies nearly 88% of the weight in the stack and nearly one-third of the manufacturing cost [6]. Therefore, the optimization of BPP can not only improve the performance of the fuel cell but also reduce the cost and weight [7]. Designing different flow field distributions can effectively improve the uniformity of the fuel and promote the removal of by-product water. The main factors to evaluate the performance of the flow field are the distribution of reactants, pressure drop loss, and the ability to prevent flooding under high current density [8].

Water management plays a critical role in the maintenance of the stable operation for PEMFC. At the gas diffusion layer-catalyst layer (GDL-CL) interface, excessive liquid water saturation will block the GDL, causing the reactant gas to fail to contact the catalyst [9, 10], a phenomenon also called flooding. There is no doubt that this will greatly reduce the output performance of the fuel cell. In addition, excellent water management is also the key to achieving uniform distribution of reactants in the gas diffusion layer and under-ribs [11]. One of the greatest challenges is water management of under-ribs (Fig. 1(d)). Usually, there is no direct airflow under the ribs to conduct liquid water. This will cause the accumulation of water under the ribs, which can completely block the gas diffusion layer above the ribs [12]. Some studies have shown that improving the mass transfer under-ribs can effectively enhance the removal of liquid water under the ribs and uniform distribution of reactants [13-15]. Therefore, the flow field designed on the principle of enhancing the convection under the ribs needs more extensive research.

Due to the low mechanical manufacturing cost and simple structure, the traditional PEMFC flow field mainly is parallel, serpentine, and interdigitated. Among them, the parallel flow field has the simplest structure. All reactants are transported in parallel channels, which have lower pumping power and total pressure drop compared to other structures. However, it is difficult for the parallel flow field to distribute the gas uniformly in the CL, and the convection under the ribs is also weak. This will cause severe flooding, which will cause uneven current density distribution and reduce the service life of the fuel cell. Compared with the parallel flow field, the serpentine flow field has a unique path from the inlet to the outlet. This feature will increase the uniformity of gas distribution, flow rate, water removal capacity, and significantly improve output power density. However, lengthy transportation routes will increase pump-

†To whom correspondence should be addressed.
E-mail: yangwm@mail.buct.edu.cn, 2019730007@mail.buct.edu.cn

ing power. In addition, as the pressure decreases near the outlet, the convection under-ribs gradually decreases, causing liquid water to accumulate that cannot be removed in time [16]. The interdigitated flow field has the best water removal capacity because of its special structure. However, this requires extremely high pumping power as a prerequisite. which will undoubtedly increase the cost of PEMFC and limit its commercial development. Therefore, researchers proposed a novel flow field design to solve these problems.

Khazaee and Ghazikhani [17] studied the influence of channel depth on the performance of straight flow field under different stoichiometric ratios by simulation and experiment. The results show that the predicted polarization curve is consistent with the experimental data. When the depths of the cathode and anode channels are 1 mm and 1.5 mm, the cell performance is best. Liu et al. proposed a new kind of flow field plate structure based on the principle of bio-inspiration and Murray's law [18]. The simulation results show that the maximum power density of the bio-inspired flow field is increased by 64.8% compared to the parallel flow field. In addition, the maximum power density of the bio-inspired flow field optimized by Murray's law is 114% higher than that of the parallel flow field. Inspired by the texture of leaves, Coban et al. designed a leaf bionic flow field [19]. The leaf flow field can effectively improve the uniformity of the gas distribution and the pressure drop values, resulting in higher power density. Compared with the standard serpentine flow field, the performance is improved up to 42.1%. The development of bionics provides a new idea for the design of the flow field. However, the structure of the bionic flow field is more complex and requires more precise dimensional control. This will increase the overall manufacturing cost of the fuel cell, which is not suitable for commercial applications. Zhang et al. [20] designed a three-dimensional flow channel to improve the uniformity of gas distribution and the removal of by-product water. The 3D flow field is designed to have wave channels, thereby increasing reaction gas from the flow channel/diffusion layer interface to the catalyst layer. This 3D flow field design introduces the concept of forced convection into the flow field distribution, which greatly improves the output performance. A large number of scholars have also conducted related studies on different 3D flow fields [21-24]. However, 3D flow fields are often accompanied by larger pressure drops and higher manufacturing costs. These will also affect the commercial development of PEMFC in the future.

Improving the output power and drainage efficiency of PEMFC by enhancing convection under-rib mass transport is also another hot research topic in flow field design [25-27]. Abdulla et al. [28] verified the positive effect of enhanced cross-flow split serpentine flow field (ECSSFF) with an active area of 55 cm^2 on the performance improvement of PEMFC. According to the simulation results, they found that the pressure drop of ECSSFF is nearly 30 times smaller than that of SSFF. This will not only reduce pump power but also reduce operating costs. Tiss et al. [29] proposed a numerical model to study the influence of under-rib convection on cell performance. They inserted some blocks in the gas channel to enhance the uniformity of the reactant gas in the GDL. This improvement enhances material transport by convection under-rib, achieving a more uniform distribution of reactants on the CL surface. Ahmed et al. [30] developed a new flow field structure based on the serpentine flow field. This flow field not only effectively enhances the under-rib mass transport but also reduces the possibility of water flooding at the GDL-CL interface. In addition, the convection under-rib can be significantly enhanced by changing the size of the flow channel and the width of the ribs in the traditional flow field [31,32]. Velisala and Srinivasulu [33] studied the effects of single, double, and triple serpentine flow field structures on the performance of PEMFC by numerical simulations and experiments. The experimental results show that, at a given inlet flow rate, the cell performance increases as the number of channels decreases. In addition, the total pressure will also be inversely proportional to the number of channels. However, most of these findings have only been simulated and not explored experimentally. This will have a great impact on the industrial application of PEMFC. In addition, some flow fields have complex structures and high processing costs, which obviously do not conform to the current research status of fuel cells.

Therefore, an EDP flow field with simple structure, low fabrication cost and excellent performance is designed in this paper. Using CFD simulation method to explore the mass transfer mechanism of EDP flow field under different parameters (flow field size, gas relative humidity, stoichiometric ratio of cathode and anode). In addition, PEMFC single-cell experiments were also performed to verify the accuracy of the simulations. The trend that the experimental and simulation results are consistent provides a reference for the industrial application of EDP flow field. Compared with the traditional flow field, the EDP flow field obtains more uniform gas distribution, higher drainage efficiency and net power density. The specific details will be described in the following chapters.

PHYSICAL MODEL DESCRIPTION

1. Geometry and Meshing

In this work, SOLIDWORKs 16.0 was used for 3D modeling. Different flow field models are shown in Fig. 1: the parallel flow field (Fig. 1(a)), the serpentine flow field (Fig. 1(b)), and the enhanced drainage parallel (EDP) flow field (Fig. 1(c)). The computational domain consists of a complete single-cell including current collector, flow field, gas diffusion layer, catalyst layer and proton exchange membrane (Fig. 2). For all simulations, the active area is fixed at 50 mm×50 mm. The thickness of the current collector, gas diffusion layer, catalyst layer, and proton exchange membrane is 2 mm, 0.12 mm, 0.01 mm, and 0.11 mm, respectively. The chan-

Table 1. Dimensions of the fuel cell

Parameter	unit	Value	References
Active area	m^2	0.0025	
Channel height	mm	1	[18]
Channel width	mm	1	[34]
Rib width	mm	1	[18]
Rib height	mm	1	
Diffusion layer thickness	mm	0.12	[18]
Catalyst layer thickness	mm	0.01	[18]
Membrane thickness	mm	0.11	[18]
Current collector thickness	mm	2	[18]

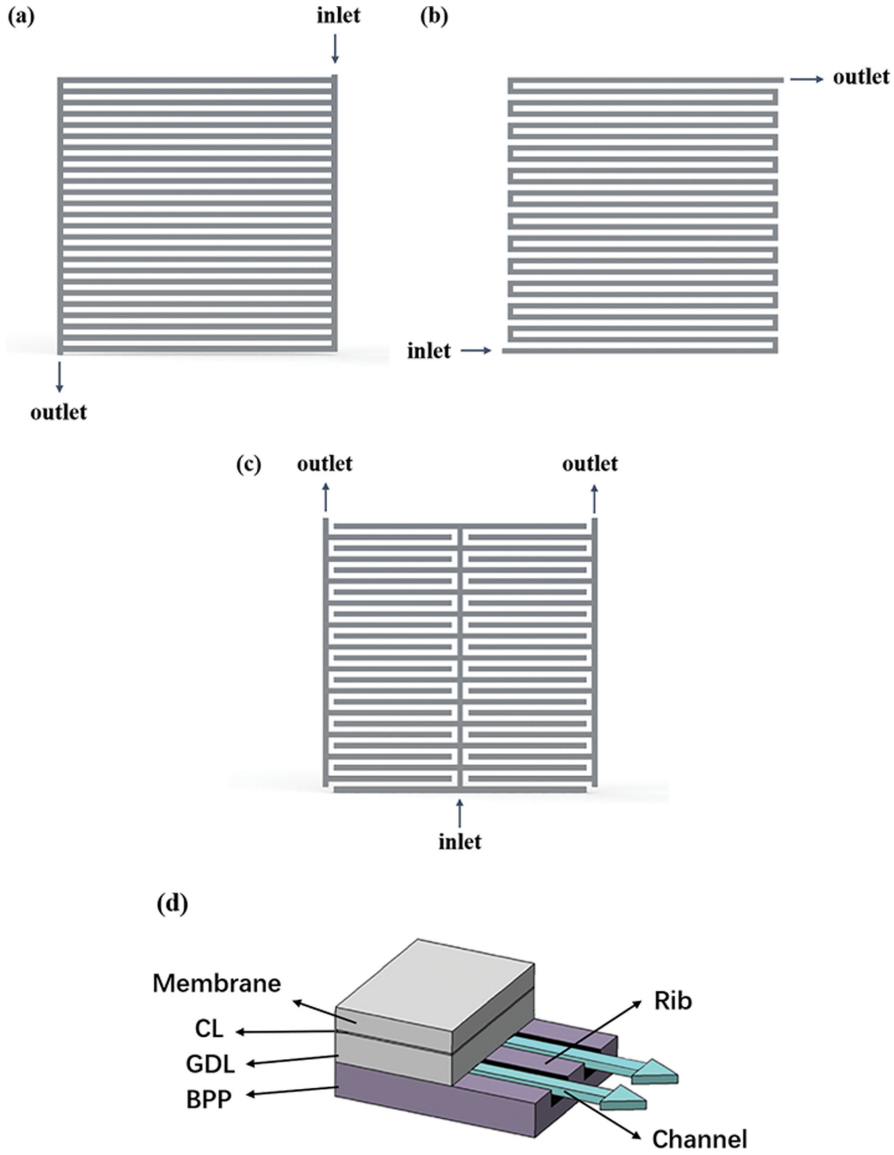

Fig. 1. Schematic diagram of flow field model: (a) parallel flow field, (b) serpentine flow field, and (c) EDP flow field. (d) Under-rib structure.

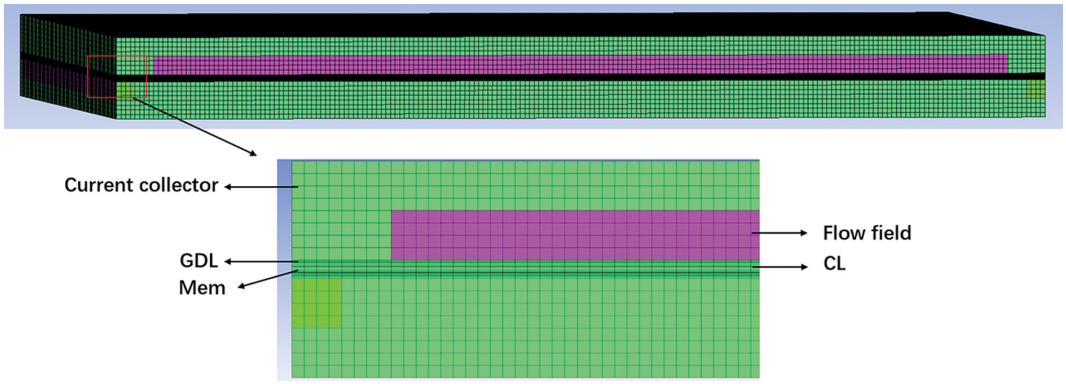

Fig. 2. Schematic diagram of computational domain and mesh topology.

nel width and rib width are both 1 mm. The specific parameters are shown in Table 1. The generated geometric model had meshed in ANSYS ICEM CFD 19.0. The mesh size was controlled by the number of nodes. The number of nodes in the bipolar plate, gas

diffusion layer, catalyst layer, and membrane thickness direction is respectively 10, 7, 5, and 5 (Fig. 2).

2. Model Assumptions

The simulation calculation includes Joule heat, reaction heat, electrochemical reaction, Butler-Volmer equation, water transport in the membrane and multiphase flow. The application of the model is based on the following assumptions:

(1) Hydrogen, nitrogen, and oxygen are all ideal gases that are insoluble in water;

(2) The influence of gravity is ignored in the whole process;

(3) Proton exchange membrane, catalyst layer, and gas diffusion layer are all isotropic materials;

(4) The state of liquid water in the flow channel is assumed to be mist, and its transmission speed is the same as that of gas.

3. Governing Equation

PEMFC simulation equations mainly include basic governing equations, electrochemical equations, and water transport equations. Among them, the basic governing equations are mass conservation equation, momentum conservation equation, energy conservation equation and composition conservation equation.

The mass conservation equation is in Eq. (1):

$$\nabla\cdot(\varepsilon\rho\vec{v})=S_m \tag{1}$$

where ε is the porosity of the porous medium, ρ is the fluid density, $\vec{v}$ is the fluid velocity vector, and S_m is the mass source term. The quality source term represents the production or consumption of reactants in each region. Since the electrochemical reaction only occurs in the catalyst layer, the quality source terms in all regions except for the catalyst layer are all zero.

The quality source term of the anode catalyst layer is in Eq. (2):

$$S_m=-\frac{M_{H_2}}{2F}R_{an} \tag{2}$$

The quality source term of the cathode catalyst layer is in Eq. (3):

$$S_m=\frac{M_{H_2O}}{2F}R_{cat}-\frac{M_{O_2}}{4F}R_{cat} \tag{3}$$

In this formula, M_{H_2}, M_{O_2}, and M_{H_2O} are the molar masses of hydrogen, oxygen and water, respectively. F is the Faraday constant. R_{an} and R_{cat} are the exchange current densities of the anode and cathode, respectively.

Momentum conservation equation in Eq. (4):

$$\nabla\cdot(\varepsilon\rho\vec{v}\vec{v})=-\varepsilon\nabla P+\nabla\cdot(\varepsilon\mu\nabla\vec{v})+S_v \tag{4}$$

In this formula, the two items on the left are the unsteady-state term and the convection term. The first two items on the right are the diffusion term, and the third term is the momentum source term. Among them, P is the pressure, μ is the dynamic viscosity, and S_v is the momentum source term. The momentum source terms in each region are all zero.

Energy conservation equation in Eq. (5):

$$\nabla\cdot(\varepsilon\rho c_p\vec{v}T)=\nabla\cdot(k\nabla T)+S_Q \tag{5}$$

where c_p is the specific heat at constant pressure, T is the temperature, k is the effective thermal conductivity, and S_Q is the energy source term.

$$S_Q=xS_{H_2O}h_{reac}+I_{area}^2R_{ohm}+r_wh_{lg}+\eta R_{an,\,cat} \tag{6}$$

where x is the ratio of chemical energy to heat energy, S_{H_2O} is water production rate, h_{reac} is electrochemical reaction enthalpy, I_{area} is surface current density, R_{ohm} is ohmic loss, r_w is water phase transition rate, h_{lg} is phase change rate of water and η is overpotential.

Composition conservation equation

$$\nabla\cdot(\varepsilon\rho\vec{v}Y_i)=D_i\nabla^2(\rho Y_i)+S_i \tag{7}$$

where i represents different components, Y_i is the volume fraction of the component, D_i is the diffusion coefficient of the component, and S_i is the component source term. Among them, the component diffusion coefficient x is obtained by the following formula.

$$D_i=\varepsilon^{1.5}(1-s)^{r_s}D_i^0\left(\frac{P_0}{P}\right)^{\gamma_p}\left(\frac{T}{T_0}\right)^{\gamma_t} \tag{8}$$

where T_0 is the reference temperature 300 K, P is the reference pressure 101,325 Pa, D_i^0 is the diffusion coefficient of the component at the reference temperature and the reference pressure, s is the water saturation, r_s is the pore-clogging index, γ_p is the pressure index, and γ_t the temperature index. The values of r_s, γ_p, γ_t are 1.0, 1.5, and 2.5, respectively. Since the electrochemical reaction only occurs in the catalyst layer, the component source terms in other regions are all zero.

In the anode catalyst layer, the component source term S_{H_2}:

$$S_{H_2}=-\frac{M_{H_2}}{2F}R_{an} \tag{9}$$

In the cathode catalyst layer, the component source terms S_{O_2} and S_{H_2O}:

$$S_{O_2}=-\frac{M_{O_2}}{4F}R_{cat} \tag{10}$$

$$S_{H_2O}=-\frac{M_{H_2O}}{2F}R_{cat} \tag{11}$$

Other related calculation equations are described in detail in our previous article [25], so we will not repeat them here.

4. Boundary Conditions

All inlet types are mass flow inlets. The anode inlet flow rate and the cathode inlet flow rate are 7.01×10^{-6} kg/s and 4.47×10^{-5} kg/s, respectively. All outlet types are pressure outlets. The operating temperature and operating pressure are 353 K and 1 atm, respectively. Set the potential of the anode current collecting plate to 0 V, and obtain the polarization curve by changing the potential of different cathode current collecting plates. The cathode and anode stoichiometric ratios were 2 and 1.5, respectively. The effective working area is set to 0.0025 m^2. The remaining parameter settings are listed in Table 2.

The commercial software ANSYS fluent 19.0 was used to solve the governing equations of momentum, continuity, energy, charge transfer, mass transfer, water transfer, and electrochemical reactions with the above boundary conditions. When solving the governing equations, to couple the flow pressure and velocity, the SIMPLE format is used. The gradient of the spatial discretization scheme is least squares cell based and the rest use the second-order discretization scheme. Cycle types all adopt F-Cycle. The criteria for termination of the multigrid cycles in solution control are used as

Table 2. Working conditions and electrochemical properties

Parameter	unit	Value	References
The porosity of the GDL		0.5	[18]
The porosity of the catalyst		0.5	[18]
Anode stoichiometry		1.5	[18]
Cathode stoichiometry		2	[18]
Operation temperature	K	353	
Operation pressure	atm	1	[18]
Relative humidity of inlet fuel	%	100	[18]
Relative humidity of inlet air	%	100	[18]
Diffusion layer viscous resistance	m^{-2}	1×10^{12}	[18]
Catalyst layer viscous resistance	m^{-2}	1×10^{12}	[18]
Hydrogen reference diffusivity	m^2/s	3×10^{-5}	[18]
Vapor reference diffusivity	m^2/s	3×10^{-5}	[18]
Oxygen reference diffusivity	m^2/s	3×10^{-5}	[18]
Other species reference diffusivity	m^2/s	3×10^{-5}	[18]
Anode exchange coefficient		2	[18]
Cathode exchange coefficient		2	[18]
Anode reference current density	A/m^2	7,500	
Anode reference concentration	$kmol/m^3$	1	[18]
Anode concentration exponential		0.5	[18]
Cathode reference current density	A/m^2	20	[18]
Cathode reference concentration	$kmol/m^3$	1	[18]
Cathode concentration exponential		1	[18]
Open-circuit voltage	V	0.95	
Anode mass flow rate	kg/s	7.01×10^{-6}	
Cathode mass flow rate	kg/s	4.47×10^{-5}	

0.001 for species and saturation equations and 0.0001 for potential equations.

5. Grid Independence Test

In order to ensure the accuracy of model calculations, we verified the grid independence of the developed model. By changing the number of nodes in the length direction, the number of control elements is 1,278,118, 1,901,908, 2,525,698, 3,149,488, and 3,796,321, respectively. Grid independence verification was carried out at 0.6 V, and the result is shown in Fig. 3. As the number of elements increases, the current density gradually stabilizes. To ensure accurate calculation and save time, we chose 2525698 as the final element quantity (each CASE requires 24 hours of computation time.).

6. Model Comparison

We compared the simulation results of this paper with the results

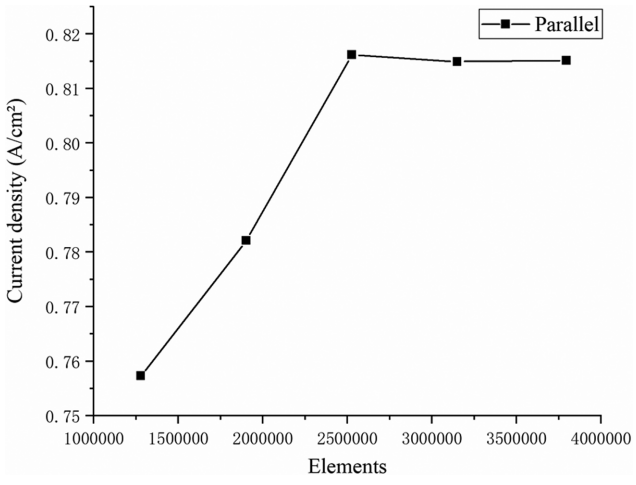

Fig. 3. Grid independence verification.

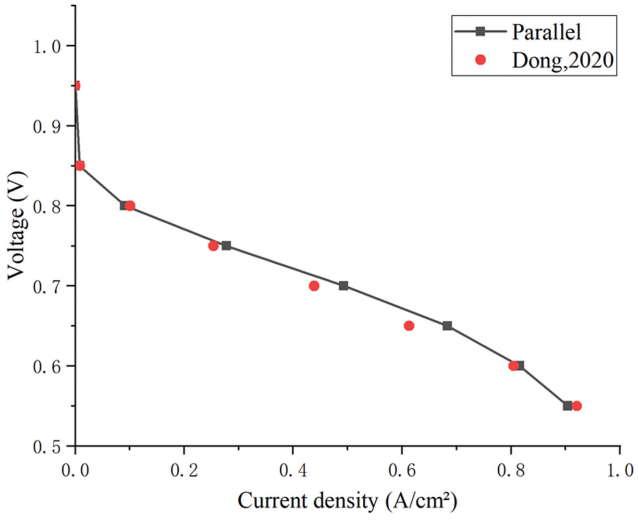

Fig. 4. Parallel flow field polarization curve model verification.

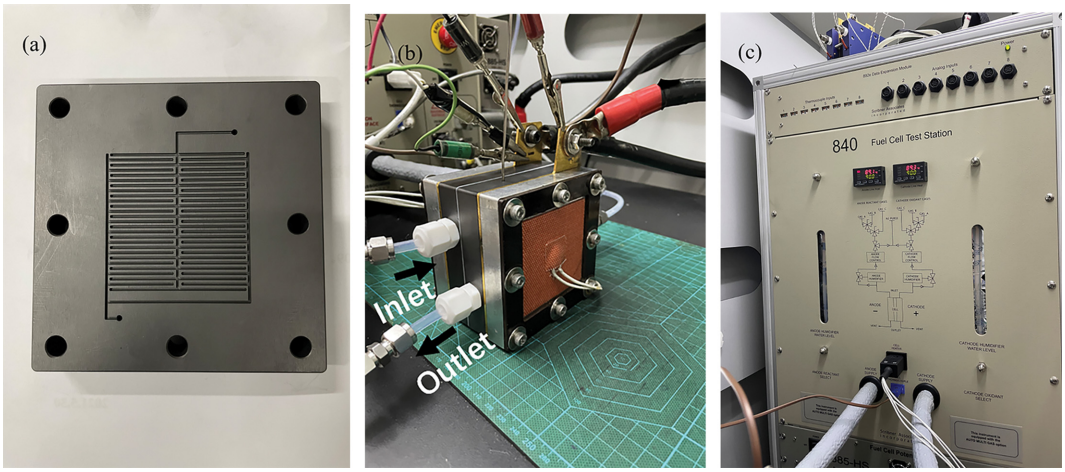

Fig. 5. (a) EDP flow field. (b) single-cell assembly diagram and (c) 840 Fuel Cell Test Station.

of Dong et al. [18]. To verify the accuracy of the model, we changed the open-circuit voltage to 1.15 V here. It can be seen from Fig. 4 that the polarization curve of our model has similar performance to the results of Dong et al. This proves the accuracy and reliability of our model. In the subsequent simulations, to approach the real operating conditions, we changed the open-circuit voltage to 0.95 V in Table 2.

EXPERIMENTAL

1. MEA Preparation

MEA was prepared by the gas diffusion electrode (GDE) method. The Pt/C catalyst (40 wt%) and Nafion ionomer solution were dispersed into the isopropanol solution by ultrasonic dispersion in proportion to prepare the catalyst ink. Then the catalyst ink was sprayed in GDL and dried to prepare for hot pressing. Finally, the catalyst-carrying GDL and Nafion 211 were hot-pressed at 130 °C for 3 minutes to complete the preparation of MEA with an active area of 25 cm^2.

2. Performance Characterization

All cell tests were performed using the 840 Fuel Cell Test Station (Fig. 5). The anode and cathode were provided by full humidified hydrogen and oxygen. The cell operating temperature was 80 °C and the back pressure was set to 0 kpa. The stoichiometric ratio of anode and cathode in the traditional flow field was 2.0. The stoichiometric ratio of the EDP flow field was 1.5 (corresponding to the simulation result). Subsequently, the anode stoichiometric ratio of the EDP flow field was controlled to 1.5, and the cathode stoichiometric ratio was gradually increased, the influence of stoichiometric ratio on cell output performance.

RESULTS AND DISCUSSION

An EDP flow field was designed to enhance mass transfer under-ribs. As shown in Fig. 1(c), the flow field is divided into three parts. The part that connects with the inlet in the middle is the main channel, which is mainly used for fuel transportation. The two independent secondary channels are blocked by the ribs in the white area. Due to the obstruction of the ribs, there will be a significant pressure difference between adjacent channels, which implies that the convection under-ribs will be enhanced. Compared with the parallel flow field, the transport of fuel in the EDP flow field is carried out from the middle to the two sides, which will significantly improve the uniformity of gas distribution in the flow field. Besides, the secondary flow channel is divided by the intermediate flow channel, which reduces the distance the water moves in the flow channel and results in faster water removal. The specific characterization will be described in detail in the following subsections. The polarization curves and power density curves of different flow fields are shown in Fig. 6.

1. Effect of EDP Flow Field on Cell Performance and Pressure Drop

The polarization and power density curves of different flow fields are in Fig. 6. As shown, all flow fields have similar performance in the low current density region (>0.7 V), which is similar to previous studies [27,30]. However, the serpentine and EDP flow fields show better performance in the high current density area (<0.7 V). A possible explanation for this might be that under high current density, concentration difference is obvious, the chemical reaction is accelerated, and a large amount of by-product water is produced at the cathode. The accumulation of a large amount of liquid water blocked the GDL and caused flooding. The parallel flow field has a small pressure drop (Fig. 6(c)) and uneven gas distribution, which makes it impossible to remove the liquid water in time. The serpentine flow field has a single transmission path, the longest distance, and the largest pressure drop (Fig. 6(c)), which can enhance water removal. However, not only is the pressure drop of the EDP flow field much lower than that of the serpentine flow field (Fig. 6(c)), but the cell performance is also better. Possibly, these results are due to the EDP flow field being divided into two parts by the rib, and there is a pressure difference between the flow channels, which enhances the removal of water from the rib. The maximum power density of the EDP flow field is 0.78 W/cm^2, which exceeds the parallel flow field and the serpentine flow field by 57% and 2.8%. This means that the EDP flow field can achieve higher power generation efficiency with less pump power loss.

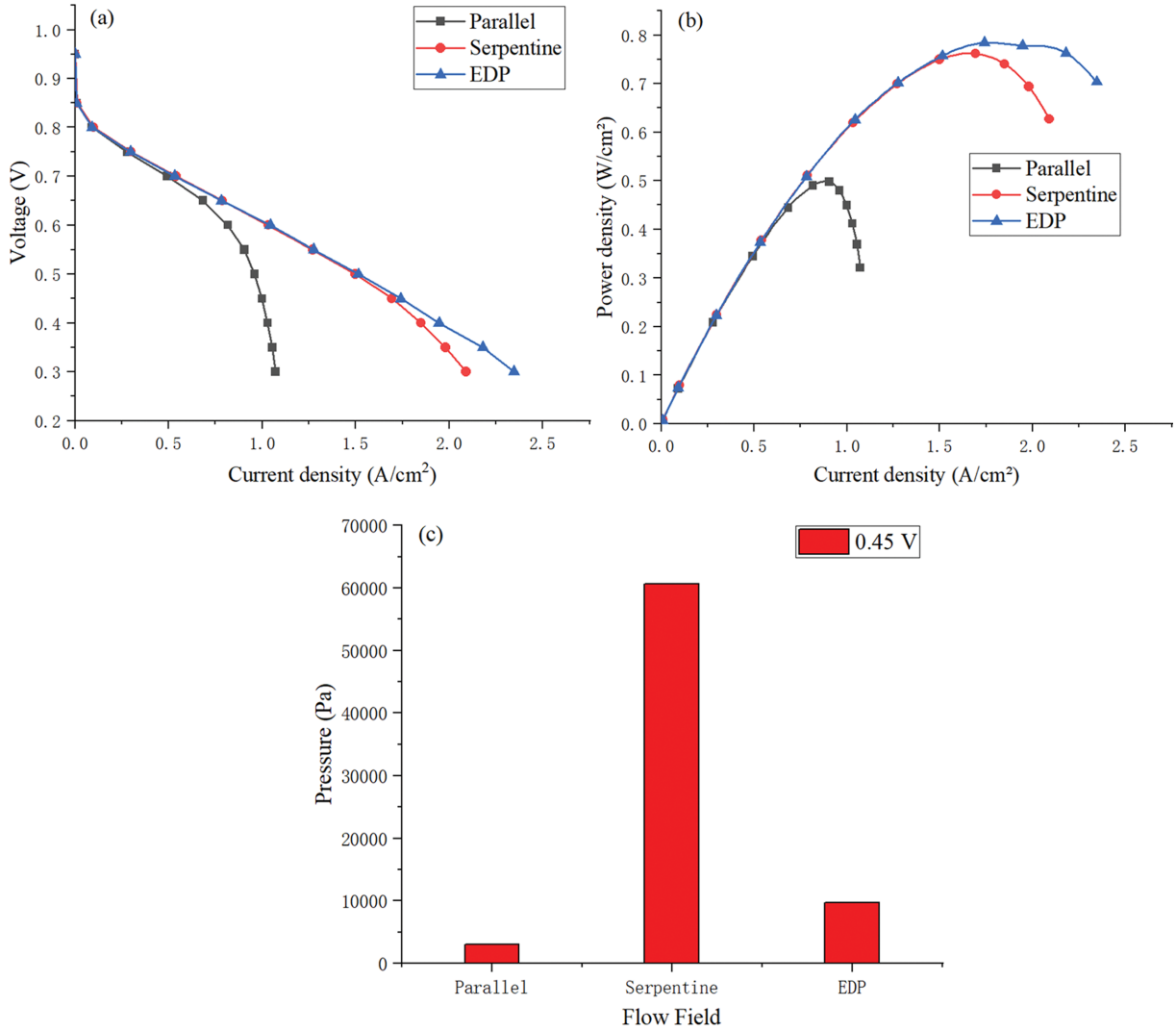

Fig. 6. (a) Polarization curves, (b) power density curves, and (c) pressure drop diagrams of different flow fields.

Table 3. EDP flow field size and power density

Name	Rib width (mm)	Channel width (mm)	Maximum power density (W/cm^2)	Increase ratio (Parallel %)	Increase ratio (Serpentine %)
Case 1	0.5	1	0.82	65.4	7.9
Case 2	1	1	0.78	57.6	2.8
Case 3	1.5	1	0.76	54.6	0.9
Case 4	1	0.5	0.46	−7.4	−39.6
Case 5	1	1.5	0.77	55.4	1.4

2. EDP Flow Field Size Optimization

Subsequently, we optimized the size of the EDP flow field, and explored the impact of rib width and flow channel width changes on cell performance. The size parameters are shown in Table 3. As shown in Fig. 7, all cases are consistent with the previous results. The maximum power density of the EDP flow field increases as the rib width decreases. When the rib width is reduced to 0.5 mm, the maximum power density can reach 0.82 W/cm^2, which exceeds the parallel flow field and serpentine flow field by 65.4% and 7.9%. It seems possible that these results are due to the smaller rib width and the shorter distance of convection under-rib. At the same inlet velocity, this will undoubtedly accelerate the speed of convective mass transfer and increase the output power. Therefore, the shorter rib width can not only enhance the convective mass transfer but also effectively reduce the pressure drop and increase the network (Fig. 7(c)). This result is also consistent with Andre et al. [12]. The pressure drop of case1 is only 5,309.9 Pa.

What is surprising is that if the channel width too small, it will

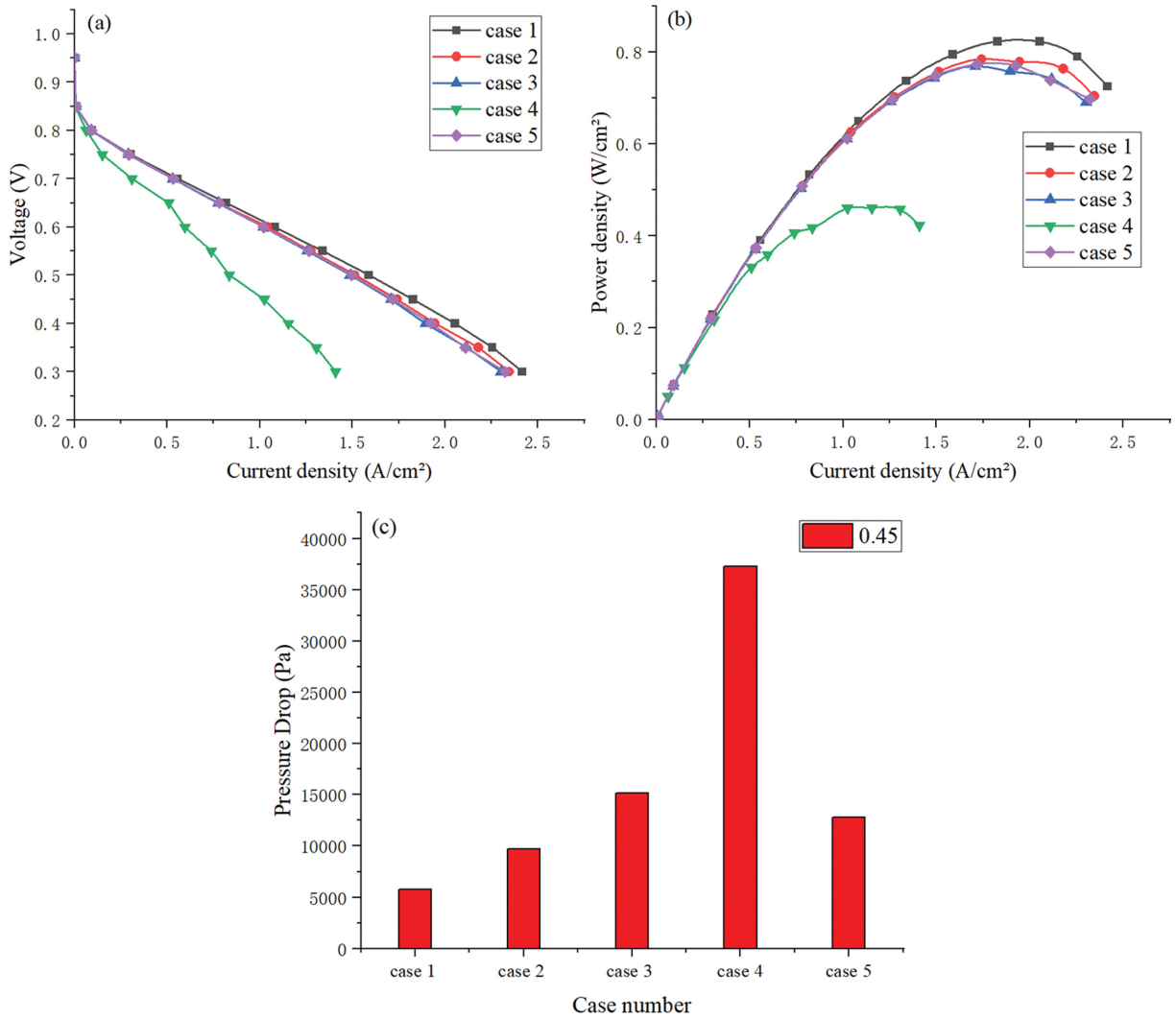

Fig. 7. (a) Polarization curve, (b) power density curve, and (c) pressure drop of EDP flow field with different rib width and channel width.

seriously affect the output power (only 0.46 W/cm^2 at 0.5 mm). Besides, the larger flow channel width will also reduce cell performance (0.77 W/cm^2 at 1.5 mm). When the width of the flow channel is too large, the gas flow rate will decrease, which may weaken the mass transfer effect under-ribs. Therefore, the use of shorter ribs (0.5 mm) and appropriate channel width (1 mm) has a positive effect on cell performance. In this work, case 1 has the best performance. The following research adopts the size parameters of case 1. In addition, subsequent investigations were carried out using the results under 0.45 V to compare the effect of the flow field on the cell performance under high current density.

3. Oxygen Mass Fraction and Water Saturation

Oxygen transport will significantly affect the performance of the fuel cell when operating in a high current density area. An increase in the reaction rate will force an increase in oxygen consumption. Therefore, a faster oxygen transport rate and more uniform local oxygen density can improve cell performance [35]. Fig. 8(a), (b), (c) shows the oxygen mass fractions of the three flow fields at the GDL-CL interface. It is apparent from Fig. 8(a) that the oxygen mass fraction under the ribs of the parallel flow field is significantly lower than that in the channel. A possible explanation for this might be that the pressure difference between adjacent channels in parallel flow fields is small, which weakens mass transfer under-ribs. Moreover, the uneven local oxygen density at the GDL-CL interface leads to worse cell performance. For the serpentine flow field (Fig. 8(c)), the oxygen mass fraction gradually decreases from the inlet to the outlet. In addition, due to the low-pressure drop near the outlet area, the mass transfer under-ribs is weak, resulting in poor oxygen content. This will cause uneven local current density and flooding [30]. However, the oxygen mass fraction distribution in the EDP flow field appears to be more uniform. Because the main flow channel and the secondary flow channel are separated by ribs, there is a significant pressure difference between adjacent flow channels. As shown in Fig. 8(b), the oxygen mass fraction under the ribs is obviously higher and more uniformly distributed (Compare with serpentine flow channel and parallel flow channel). Besides, the oxygen mass fraction gradually decreases from the inlet of the main channel to the end. However, except for the lower oxygen content at the end of the main channel, there is no big difference in oxygen content in other regions. Obviously, the EDP flow field not only improves

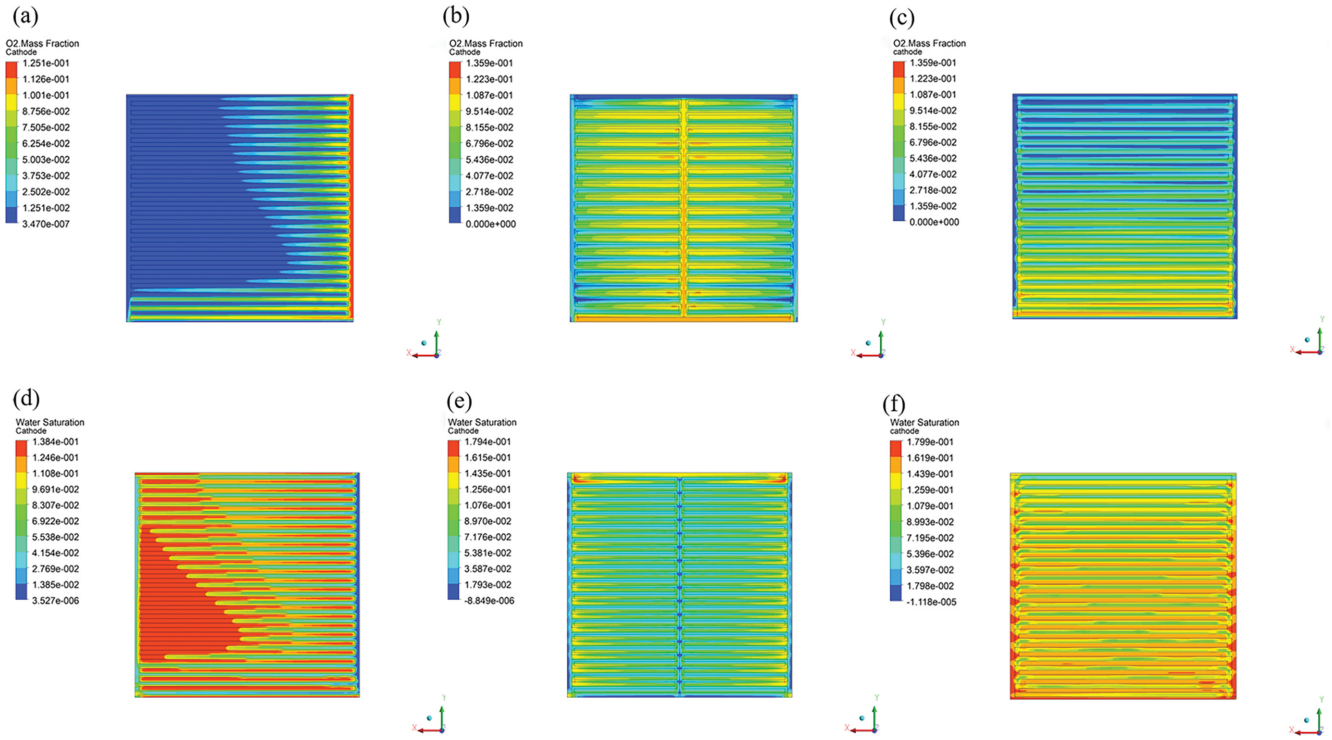

Fig. 8. The oxygen mass fraction and water saturation of (a), (d) parallel, (b), (e) EDP, and (c), (f) serpentine flow field.

the oxygen mass distribution under-ribs but also improves the oxygen content in the channel. This is also consistent with the previous polarization curve results, verifying that a more uniform oxygen distribution can effectively increase the output power of the fuel cell.

Excessive water saturation of the gas diffusion layer will cause flooding, block the porous structure, and increase the fuel transmission resistance. At a specific current density and water production rate, the lower value of liquid water saturation can be attributed to the rapid removal of by-product water from the reaction site [36]. The water saturation at the GDL-CL interface is shown in Fig. 8(d), (e), (f). It can be seen from the color that the red area of the traditional flow field is more than that of the EDP flow field, which leads to serious flooding. The lower inlet pressure, short channel path, and weak convection under the ribs are the main reasons for the high water saturation of the parallel flow field. Compared with the parallel flow field, the serpentine flow field has a longer channel and a larger inlet pressure. However, excessive turning angles cause local turbulence, which affects the removal of water [16]. Also, insufficient pressure at the end of the channel is one of the main reasons for local flooding. However, the water saturation distribution of the EDP flow field (Fig. 8(e)) is mainly light blue and green, showing extremely low water saturation. Through

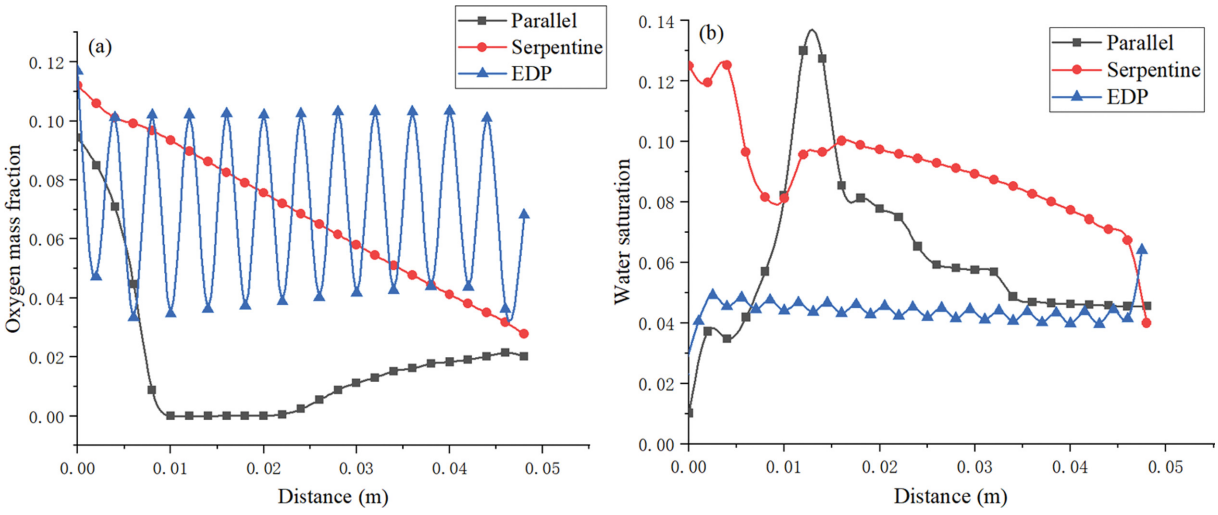

Fig. 9. The linear distribution of (a) oxygen mass fraction and (b)water saturation at the CDL-CL interface (X=0.01 m, Z=0.00125 m).

the change of the flow field structure, the free diffusion of oxygen is transformed into convective mass transfer diffusion. The high pressure of the main flow channel forces the by-product water into the drainage channel and removes it from the reactive zone. This allows the EDP flow field to maintain high and stable performance in the high current density area, which is also consistent with the previous oxygen mass fraction distribution results.

We chose a straight line under the same coordinates in the active area to obtain the oxygen mass fraction and water saturation values of different flow fields. The results are shown in Fig. 9. As shown in Fig. 9(a), the oxygen content of the serpentine flow field gradually decreases from the inlet to the outlet, which is consistent with the result of Fig. 8(c). The oxygen mass fraction of the parallel flow field gradually decreases from the inlet, then remains stable at the lowest point, and finally increases slightly. It seems possible that these results are due to being blocked close to the outlet, forcing the gas to travel to the left channel. As a result, the oxygen mass fraction rises at the end of the channel. The oxygen distribution in the EDP flow field has obvious periodic changes. These results are likely to be related to the fuel transfer channels separated by ribs. However, the uniformity of oxygen distribution in the EDP flow field is significantly higher than that of the traditional flow field. The water saturation of the EDP flow field (Fig. 9(b)) is not only much lower than the traditional flow field but also more uniform, which is consistent with the previous results. These results also further confirm that the EDP flow field has better drainage performance and more uniform reaction gas distribution.

4. Current Density and Pressure

Fig. 10(a), (b), (c) is a count of the current density distribution for three flow fields in the middle part of the membrane. As shown in Fig. 10(a), the current density distribution of the parallel flow field is not uniform, and there are large blue areas of low current density. We found that areas with low oxygen mass fraction (Fig. 8(a)) and high water saturation (Fig. 8(d)) have lower current density. This result also proves our previous conclusion that the higher the water saturation, the greater the oxygen transmission resistance. As a result, the porous layer is blocked, oxygen cannot contact the catalyst to react, and the current density decreases. In addition, a similar situation occurs in the serpentine flow field (Fig. 10(c)), where the current density is low and the distribution is obviously uneven. However, the EDP flow field shows a higher current density and a more uniform distribution. The current density gradually decreases from the main channel in the middle to both sides, which is consistent with the previous results (Fig. 8(b), (e)). These results further support the idea that the EDP flow field can obtain a more uniform fuel distribution and better water removal effect by enhancing the convection under-ribs. Fig. 10(d), (e), (f) shows the pressure distribution of the channel. The parallel flow field (Fig. 10(d)) and the serpentine flow field (Fig. 10(f)) show a common characteristic, which is the pressure gradually decreases from the inlet to the outlet. However, the EDP flow field exhibits a different pressure distribution due to the particularity of the structure. As shown in Fig. 10(e), the pressure in the main channel is significantly higher than that in the secondary channel. This pressure difference is the main reason for the enhancement of convection under-ribs. Besides, whether it is the main channel or the secondary channel, the uniformity of the pressure distribution is also better than that of the traditional flow field. This result also

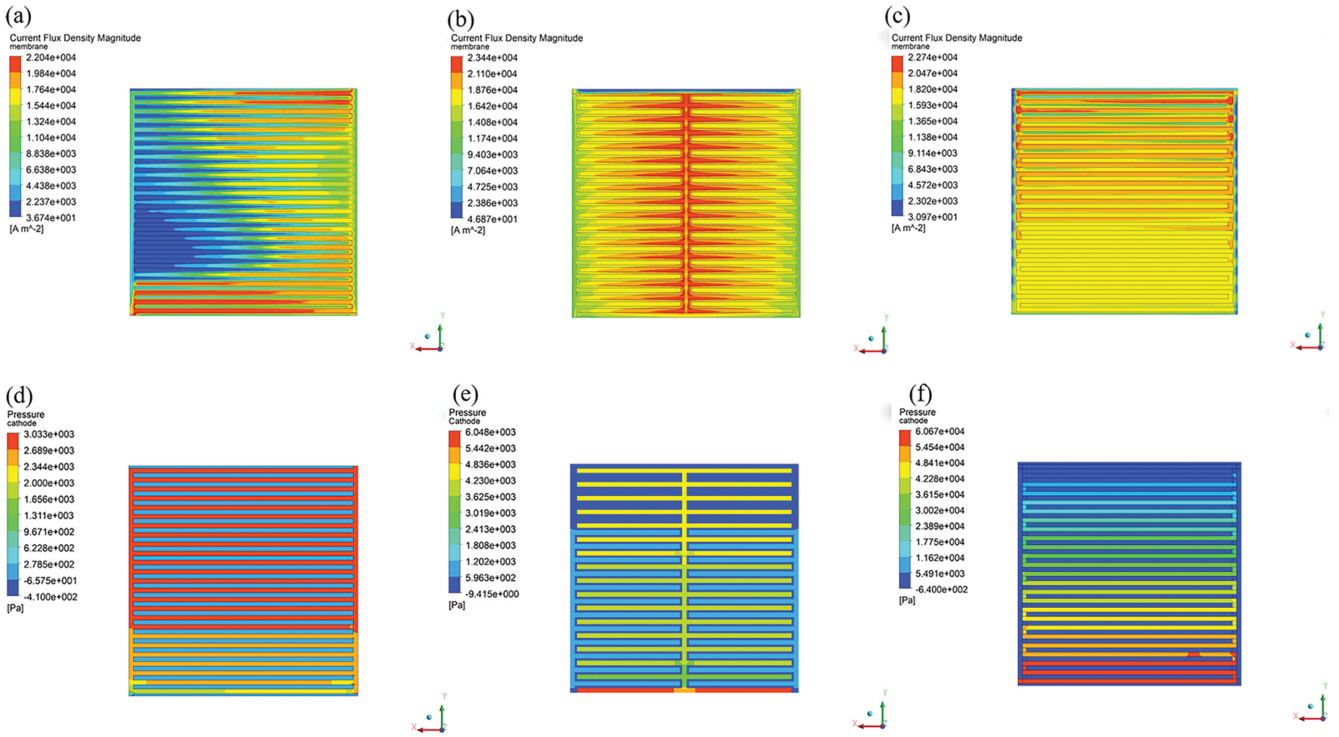

Fig. 10. (a) Parallel, (b) EDP, and (c) serpentine flow field current density distribution in the middle part of the membrane. (d) Parallel, (e) EDP, and (f) serpentine flow field pressure distribution in the flow.

confirms that changing the pressure of adjacent flow channels can achieve better mass transfer effects under the ribs.

5. Relative Humidity and Stoichiometric Ratio

Fig. 11(a), (b) shows the polarization curve and power density curve of the EDP flow field under different relative humidity (RH). When reducing the cathode RH, the anode maintains 100% RH and vice versa. It can be seen from Fig. 11(a), (b) that whether it is reducing the cathode RH or the anode RH, it will lead to a decrease in cell performance. A possible explanation for this might be that the decrease in relative humidity will affect the conductiv-

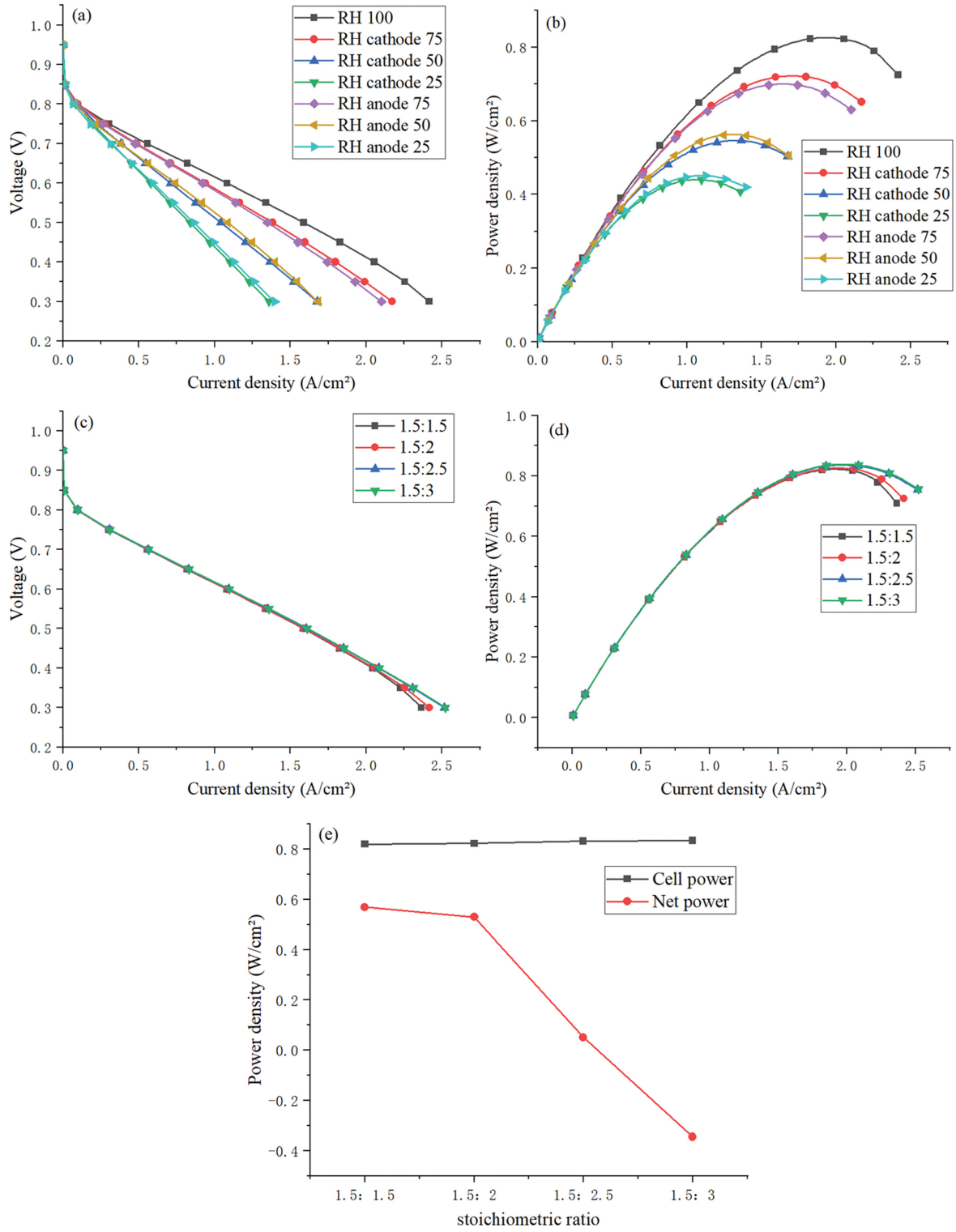

Fig. 11. (a) Polarization curve and (b) power density curve for different relative humidity. (c) Polarization curves, (d) power density curves, and (e) net power curves for different cathode stoichiometric ratios.

ity of the membrane to protons, thereby affecting the efficiency of the chemical reaction [37]. Therefore, maintaining 100% RH in this work can maximize the output performance. An increase in the cathode stoichiometric ratio often leads to higher output power [38]. However, an excessively large stoichiometric ratio will increase more pump power, resulting in a decrease in net power. We calculated the pump power and net power under different cathode stoichiometric ratios according to the formula in the literature [39] and listed the values in Table 4. As shown in Fig. 11(c), (d), (e), as the cathode stoichiometric ratio increases, the maximum power density is increased. Compared with the power density, the pressure drop is increased by a greater extent. When the cathode stoichiometric ratio is 3, the pressure drop reaches 13,401 Pa. Therefore, only through the comparison of net power can the best stoichiometric ratio be determined. As shown in Fig. 11(e), when the stoichiometric ratio is 1.5 (anode): 1.5 (cathode), the net power reaches the maximum, even if its power density is not the maximum. In this work, considering the loss of pump power, the best stoichiometric ratio is 1.5 (anode): 1.5 (cathode).

6. Experimental Result

The results of the single-cell experiment are shown in Fig. 12. The performance of all flow fields has been improved in actual tests. This result can be explained by the higher activity of our MEA (high Pt loading). In addition, we used pure oxygen instead of air in the

Table 4. Cathode stoichiometric ratio and net power

Anode relative humidity (RH)	Cathode relative humidity (RH)	Anode stoichiometric ratio	Cathode stoichiometric ratio	Pressure (Pa)	Net power (Wcm^{-2})
100%	100%	1.5	1.5	5,309.9	0.56
100%	100%	1.5	2	5,798.4	0.52
100%	100%	1.5	2.5	10,378.3	0.05
100%	100%	1.5	3	13,401	−0.34

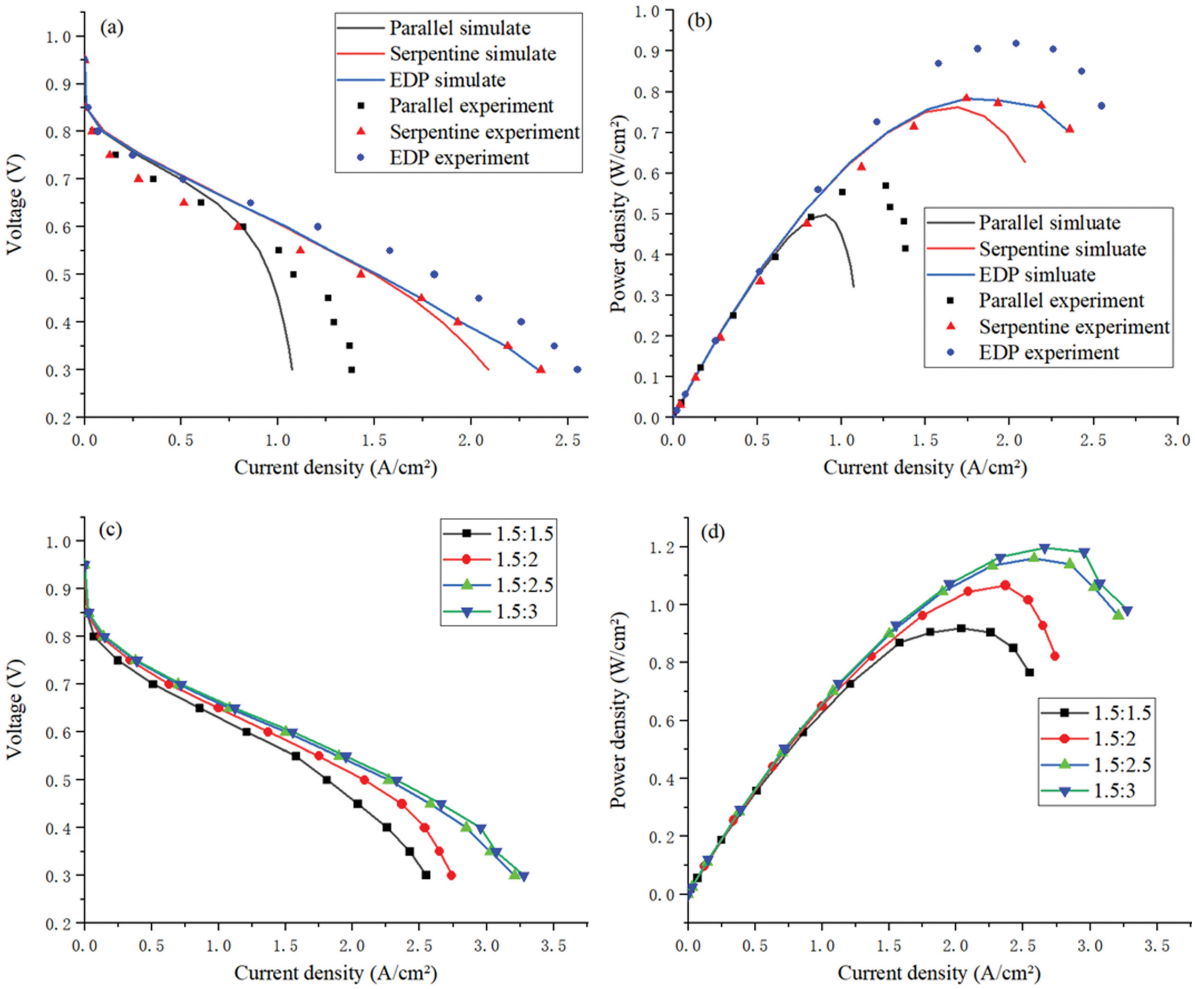

Fig. 12. Experimental and simulate (a) polarization curve and (b) power density curve comparison chart. Polarization curves (c) and power density (d) curves at different cathode stoichiometric ratios in the EDP flow field experiment.

experiment, which will undoubtedly improve our cell performance. In the cell assembly process, different process operations will also affect the output performance. Even if the performance is improved, the EDP flow field still has the best performance. As shown in Fig. 12(b), the maximum power density (0.91 W/cm^2) of the EDP flow field (rib: 0.5 mm, channel: 1 mm) is 61% and 17% higher than the parallel flow field (0.56 W/cm^2) and the serpentine flow field (0.78 W/cm^2), respectively. This further verified from the experimental results that the EDP flow field has the best performance and the reliability of the simulation results. When the cathode stoichiometric ratio of the EDP flow field was increased, the output performance of the cell also received positive feedback (Fig. 12(c), (d)). This experimental result is also consistent with our previous simulation results. Furthermore, when the stoichiometric ratio was 1.5 : 3, the maximum power density of the EDP flow field was as high as 1.19 W/cm^2. An increase in the cathode stoichiometric ratio will speed up the reaction rate and increase the production of by-product water [13]. However, the characteristics of the EDP flow field structure will significantly accelerate the rate of drainage (double-sided drainage, shorter distance), so that the cell avoids flooding and maintains stable operation.

CONCLUSION

The EDP flow field model was designed on the principle of enhancing convection under-ribs. In high current density areas where flooding is more serious, the EDP flow field not only improves the uniform distribution of fuel, but also enhances the removal efficiency of water under the ribs. Compared with the parallel flow field and the serpentine flow field, the maximum power density of the EDP flow field was increased by 69.4% and 7.9%, respectively. This study has shown that when the width of the ribs is reduced, the output power of the cell can be effectively increased (0.5 mm, 0.82 W/cm^2). In addition, the relative humidity of the anode and cathode had a significant impact on cell performance. As the relative humidity decreased, the power density of the cell gradually decreased. In this work, we determined that the best relative humidity of the cathode and anode is 100%. According to the simulation results, we found that as the cathode stoichiometric ratio increases, the pressure drop and pump power will also increase. Under optimal conditions, the net power of the EDP flow field was as high as 0.56 W/cm^2. The pressure drop of the EDP flow field was much lower than that of the serpentine flow field (EDP: 5,309.9 Pa, serpentine: 60,670 Pa), but it can achieve a higher power density. In addition, the results of the single-cell experiment also show a consistent trend with the simulation results and the experimental performance is better. In the final experimental results, when the cathode stoichiometric ratio was 3, the maximum power density of the EDP flow field was as high as 1.19 W/cm^2. This means that the EDP flow field has great potential in commercial applications. Therefore, the EDP flow field can be considered as a possible alternative to the traditional flow field design.

ACKNOWLEDGEMENT

The authors gratefully acknowledge the financial support of the National Key R & D Program of China: 2016YFB0302000.

NOMENCLATURE

S_m : source term for mass [kg m^{-3}s^{-1}]
ε : porosity [-]
ρ : density [kg m^{-3}]
M_i : molecular mass of species [g mol^{-1}]
$R_{an,cat}$: volumetric transfer current [A m^{-3}]
F : faraday constant [C mol^{-1}]
μ : viscosity [kg m^{-1}s^{-1}]
T : temperature [K]
c_p : constant-pressure specific heat [J kg^{-1}K^{-1}]
k^{eff} : effective thermal conductivity [W·m^{-1}·K^{-1}]
S_Q : source term for energy [W m^{-3}]
I_{area} : surface current density [A·m^{-2}]
R_{ohm} : ohmic loss [Ω]
h_{lg} : phase change enthalpy of water [kJ·kg^{-1}]
h_{rea} : reaction enthalpy [kJ mol^{-1}]
x : ratio of chemical energy to heat energy
r_w : phase change rate (condensation/evaporation) [kg m^{-3}s^{-1}]
S_i : source term of species [kg m^{-3}s^{-1}]
Y_i : volume fraction of the species [-]
D_i : gaseous diffusivity of species *i* [m^{2}s^{-1}]
D_i^0 : mass diffusivity of species at reference temperature and pressure (P_0, T_0) [m^{2}s^{-1}]
P : pressure [Pa]
s : water saturation [-]

REFERENCES

1. P. Yi, D. Zhang, D. Qiu, L. Peng and X. Lai, *Int. J. Hydrogen Energy*, **44**, 6813 (2019).
2. W. Zhu, J.-a. Fang, W. Zhang, Y. Xu and L. Tong, *Arabian J. Sci. Eng.*, **39**, 2869 (2014).
3. H. Kahraman, I. Cevik, F. Dündar and F. Ficic, *Arabian J. Sci. Eng.*, **41**, 1961 (2016).
4. C. A. Idibie, S. A. Abdulkareem, C. Pienaar, S. E. Iyuke and L. Vandyk, *Ind. Eng. Chem. Res.*, **49**, 1600 (2010).
5. Y. Amadane, H. Mounir, A. E. Marjani, H. Bouhrim and M. A. Rafi, *Arabian J. Sci. Eng.*, **45**(9), 7587 (2020).
6. S. Abdulla and V. S. Patnaikuni, *Int. J. Hydrogen Energy*, **45**, 25970 (2020).
7. M. F. Pefeer, O. N. Cora and M. Kog, *Int. J. Hydrogen Energy*, **36**, 15427 (2011).
8. B. Randrianarizafy, P. Schott, M. Chandesris, M. Gerard and Y. Bultel, *Int. J. Hydrogen Energy*, **43**, 8907 (2018).
9. M. El-Dosoky, M. Ahmed and N. Ashgriz, *Int. J. Energy Res.*, **42**, 1664 (2018).
10. I. Khazaee and M. Ghazikhani, *Arabian J. Sci. Eng.*, **38**, 2521 (2013).
11. B. H. Lim, E. H. Majlan, W. R. W. Daud, T. Husaini and M. I. Rosli, *Ionics*, **22**, 1 (2016).
12. I. Khazaee and M. Ghazikhani, *Arabian J. Sci. Eng.*, **38**, 1551 (2013).
13. D. Gerteisen, T. Heilmann and C. Ziegler, *J. Power Sources*, **187**, 165 (2009).
14. L. Xuan, G. Hang, Y. Fang and F. M. Chong, *Electrochim. Acta*, **52**,

3607 (2007).
15. K. Prasad and S. Jayanti, *J. Power Sources*, **180**, 227 (2008).
16. A. Arvay, J. French, J. C. Wang, X. H. Peng and A. M. Kannan, *Int. J. Hydrogen Energy*, **38**, 3717 (2013).
17. I. Khazaee and M. Ghazikhani, *Arabian J. Sci. Eng.*, **37**, 2297 (2012).
18. J. Dong, S. Liu and S. Liu, *J. Renew. Sustain. Energy*, **12**, 044303 (2020).
19. H. Kahraman and A. Coban, *Arabian J. Sci. Eng.*, **45**, 5143 (2020).
20. X. Yan, C. Guan, Y. Zhang, K. Jiang, G. Wei, X. Cheng, S. Shen and J. Zhang, *Appl. Therm. Eng.*, **147**, 1107 (2019).
21. T. Yoshida and K. Kojima, *Electrochem. Soc. Interface*, **24**, 45 (2015).
22. H. Heidary, M. J. Kermani and B. Dabir, *Energy Convers. Manage.*, **124**, 51 (2016).
23. S. W. Perng and H. W. Wu, *Appl. Energy*, **143**, 81 (2015).
24. V. Velisala, G. Pullagura, N. Yarramsetty, S. Vadapalli and K. K. Gorantla, *Arabian J. Sci. Eng.*, **46**(12), 11687 (2021).
25. H. C. Liu, W. M. Yang, L. S. Cheng and J. Tan, *Fuel Cells*, **18**, 173 (2017).
26. Z. Shi and W. Xia, *J. Power Sources*, **185**, 985 (2008).
27. G. Hang, P. C. Yue, Q. X. Yan, Y. Fang and F. M. Chong, *Int. J. Hydrogen Energy*, **38**, 11028 (2013).
28. S. Abdulla, M. M. Seepana and V. S. Patnaikuni, *Arabian J. Sci. Eng.*, **45**, 7691 (2020).
29. F. Tiss, R. Chouikh and A. Guizani, *Energy Convers. Manage.*, **80**, 32 (2014).
30. F. B. Baz, S. Ookawara and M. Ahmed, *Int. J. Hydrogen Energy*, **44**, 30644 (2018).
31. S. Shimpalee and J. Zee, *Int. J. Hydrogen Energy*, **32**, 842 (2007).
32. M. Z. Chowdhury, O. Genc and S. Toros, *Int. J. Hydrogen Energy*, **43**, 10798 (2018).
33. V. Velisala and G. N. Srinivasulu, *Arabian J. Sci. Eng.*, **43**, 1225 (2018).
34. S. Abdulla and V. S. Patnaikuni, *Int. J. Energy Res.*, **43**, 2806 (2019).
35. F. Barbir, A. Boston, H. London, N. York and S. Tokyo, Elsevier Academic Press (2005).
36. W. Li, Q. Zhang, C. Wang, X. Yan, S. Shen, G. Xia, F. Zhu and J. Zhang, *Appl. Energy*, **195**, 278 (2017).
37. E. Celik and I. Karagoz, *J. Power Energy*, **234**, 1189 (2020).
38. R. Liu, W. Zhou, S. Li, F. Li and W. Ling, *Int. J. Hydrogen Energy*, **45**, 17833 (2020).
39. H. Liang, H. A. Ming, B. Yga, B. Dfa, B. Pwa, L. Bo and A. Zs, *Energy Convers. Manage.*, **205**, 112335 (2020).